instruments

MDPI

Article

Characterization and Pilot Human Trial of Dedicated Breast Ring Positron Emission Tomography (BRPET) System

Andrew M. Polemi [1,2,*], Annie K. Kogler [3], Patrice K. Rehm [1], Luke Lancaster [1], Heather R. Peppard [1], Patrick M. Dillon [4], Alexander V. Stolin [5], Stanislaw Majewski [1] and Mark B. Williams [1,2,3]

1 Department of Radiology and Medical Imaging, University of Virginia, Charlottesville, VA 22908, USA; pkr3b@virginia.edu (P.K.R.); LL6V@hscmail.mcc.virginia.edu (L.L.); heather.peppard@va.gov (H.R.P.); stan.majewski@gmail.com (S.M.); mbwilliams@virginia.edu (M.B.W.)
2 Department of Biomedical Engineering, University of Virginia, Charlottesville, VA 22908, USA
3 Department of Physics, University of Virginia, Charlottesville, VA 22904, USA; akk68@drexel.edu
4 Department of Medicine, University of Virginia, Charlottesville, VA 22908, USA; pmd5b@hscmail.mcc.virginia.edu
5 Department of Radiology, West Virginia University, Morgantown, WV 26506, USA; astolin@hsc.wvu.edu
* Correspondence: amp3as@hscmail.mcc.virginia.edu

Abstract: We describe the design and performance of BRPET, a novel dedicated breast PET (dbPET) scanner designed to maximize visualization of posterior regions of the breast. BRPET uses prone imaging geometry and a 12-module detector ring built from pixelated LYSO crystals coupled to position sensitive photomultiplier tubes (PSPMTs). Optical coupling via slanted plastic fiber optic light guides permits partial insertion of the crystals into the exam table's breast aperture. Image quality testing procedures were adapted from the NEMA NU4-2008 protocol. Two additional phantom tests quantified the posterior extent of the usable volume of view (VoV). BRPET axial, radial, and tangential FWHM spatial resolutions at the isocenter were 1.8, 1.7, and 1.9 mm, respectively. The peak absolute system sensitivity was 0.97% using an energy window of 460–562 keV. The peak noise equivalent counting rate was 5.33 kcps at 21.6 MBq. The scanner VoV extends to within ~6 mm of the plane defining the location of the chest wall. A pilot human study (n = 10) compared the diagnostic performance of FDG-BRPET to that of contrast enhanced MRI (CEMRI), with biopsy as ground truth. Averaged over three expert human observers, the sensitivity/specificity for BRPET was 0.93/1.0, compared to 1.0/0.25 for CEMRI.

Keywords: dedicated breast PET; performance evaluation; PET instrumentation; breast imaging

Citation: Polemi, A.M.; Kogler, A.K.; Rehm, P.K.; Lancaster, L.; Peppard, H.R.; Dillon, P.M.; Stolin, A.V.; Majewski, S.; Williams, M.B. Characterization and Pilot Human Trial of Dedicated Breast Ring Positron Emission Tomography (BRPET) System. *Instruments* **2021**, *5*, 30. https://doi.org/10.3390/instruments5030030

Academic Editor: Antonio Ereditato

Received: 23 July 2021
Accepted: 2 September 2021
Published: 10 September 2021

1. Introduction

Whole body PET (WBPET) using the radiotracer FDG is being increasingly utilized in breast cancer diagnosis, staging, and evaluation of treatment response [1–3]. Over the past 25 years, interest in the detection of smaller, earlier stage breast cancers has led to the development of a number of dedicated breast PET (dbPET) scanners with improved spatial resolution compared to WBPET. The first dbPET systems used two opposing planar detectors between which the breast was compressed [4]. The PEM Flex Solo II breast PET scanner, marketed by Naviscan (CMR Naviscan, Carlsbad, CA, USA), uses two opposing rectangular planar detectors that are scanned in synchrony in the left–right direction above and below the compressed breast [5]. Its in-plane spatial resolution of ~2.4 mm has been shown to lead to increased sensitivity for detection of small lesions [6,7]. However, the limited angular span of the lines of response (LORs) available with the static opposing planar detector geometry result in tomosynthesis-like limited angle acquisition and therefore poorer spatial resolution in the direction normal to the detector surfaces [5].

For more isotropic spatial resolution, dbPET/CT systems have been developed that use one or more pairs of opposing planar detectors on a rotation stage for step-and-shoot

image acquisition over 180° [8,9]. Shimadzu (Kyoto, Japan) developed semi-prone full ring (O-PET) and partial ring (C-PET) systems, both designed to provide nearly isotropic spatial resolution while improving photon sensitivity [10,11]. Two prone, full-ring commercial systems have recently become available; the MAMMI system from Oncovision (Valencia, Spain) [12] and the Elmammo system from Shimadzu [13,14].

Human studies of dbPET systems have found that visualization of posterior breast tissue is often poor because unlike WBPET, the dbPET geometry places the posterior breast at the boundary of the volume of view (VoV), where the probability of coincident events, and thus photon sensitivity, approaches zero. The problem can be further exacerbated in prone imaging systems due to the thickness of the table, which has the effect of pushing the posterior breast region further out of the VoV. While each of the above dbPET systems, with spatial resolutions ranging from 1 to 2.5 mm FWHM [8,10,12,13], successfully improved the resolution compared to WBPET systems, only the C-shaped Shimadzu system was specifically designed with the goal of improving visualization of posterior breast tissue [10].

In an attempt to improve the visualization of the posterior breast tissue compared to previous dbPET scanners, the breast ring PET (BRPET) system was developed and tested in a collaborative effort among the University of Virginia, West Virginia University, and the Jefferson Lab (Newport News, VA, USA). The BRPET dbPET scanner comprises a single 12-module PET ring mounted below a Lorad prone biopsy table.

The following sections present the characterization of the BRPET imaging performance, as well as the results of a pilot human study comparing BRPET to contrast-enhanced MRI (CEMRI).

2. Materials and Methods

2.1. Scanner Design

The BRPET ring (inner diameter 20.5 cm) is mounted on the vertical translation stage originally used for the X-ray tube and detectors of the Lorad biopsy system (Hologic Inc., Marlborough, MA, USA), so that the vertical ring positions can be adjusted for complete breast coverage with adequate SNR (Figure 1). Images from each ring position are reconstructed separately and then stitched together.

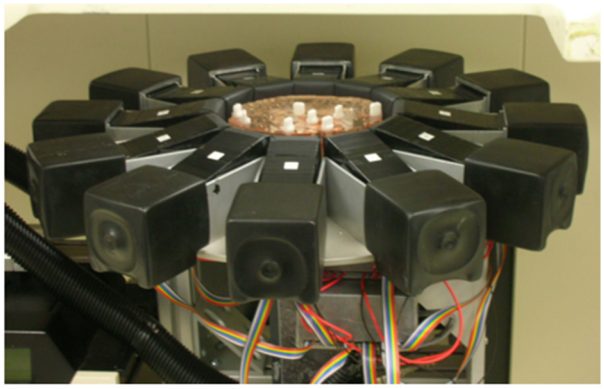

Figure 1. BRPET ring with slanted light guides labeled with white squares. The ring is attached below the breast aperture of a modified Lorad biopsy table.

Each of the ring's 12 modules contains a 24 × 24 array of LYSO scintillator crystals (Proteus, Inc., Chagrin Falls, OH, USA). Each crystal is 2 × 2 × 10 mm thick, and the crystal pitch is 2.1 mm. The array is optically coupled to a Hamamatsu H8500 PSPMT (active area of 49 × 49 mm; bialkali photocathode; an 8 × 8 discrete anode array; Hamamatsu Photonics, Hamamatsu City, Shizuoka, Japan), using a fiberoptic light guide. The fiberoptic light guide comprises 22 × 22 glued bundle of tightly packed round 2 mm diameter plastic optical fibers (Saint-Gobain BCF-98) with polystyrene-based cores (refractive index = 1.60), and PMMA cladding (refractive index = 1.49). In order to keep the fiber bunch mechanically together, maximize scintillation light propagation in the fibers, and minimize cross talk

between fibers, the inter-fiber gaps are filled with optical cement with a transmission of >98% for wavelengths above 400 nm (Saint-Gobain Crystals, Malvern, PA, USA). The slanted light guide offsets the scintillation crystal array 12 mm vertically upward relative to the PSPMT, so that it extends partially into the breast aperture (Figure 2). This vertical shift is designed to maximize imaging of posterior breast tissue [15].

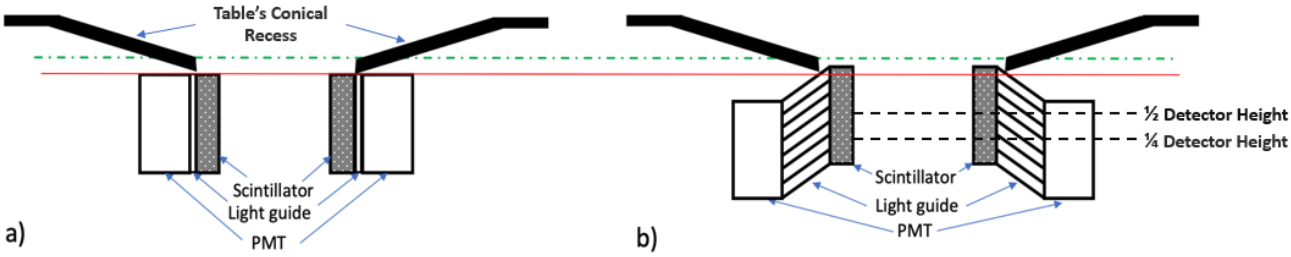

Figure 2. Schematic illustration of the slanted light guide geometry. (**a**) classic detector module design using thin, straight light guides to couple scintillator and PMT; (**b**) the module design used in the BRPET scanner, including the thicker slanted light guides. The dotted green line represents the top surface of the hole in the ventral end of the table's conical recess, and the red line indicates the physical limitation of the classic design.

Each module has the manufacturer-provided PSPMT board providing connections for high voltage (HV), final stage dynode output, and 64 individual anode outputs. High voltage from a single power supply first goes to a separate board containing 12 trim potentiometers to permit adjustment of the HV going to each PSPMT to equalize gain among modules. Attached to each factory PSPMT board is custom designed (Jefferson Lab, Newport News, VA, USA) resistive matrix circuit board whose resistor values are selected to compensate for gain nonuniformities over the PSPMT active area [16]. A final board converts the 64-channel individual anode readout first to 16 channels (8X $\times$ 8Y) and then to X+, X−, Y+ and Y− outputs for position encoding. The X and Y coordinate data from all 12 modules (48 total) are sent to a 64-channel integrating analog-to-digital converter (ADC) (AiT Instruments, Newport News, VA, USA) (see Figure 3).

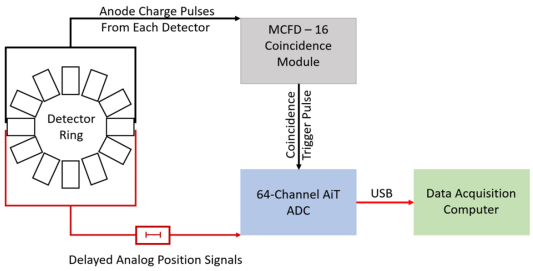

Figure 3. Schematic of the BRPET systems data acquisition system.

The charge pulses, summed over the 64 individual PSPMT anodes, from each of the twelve detector modules are fed to a Mesytec 16-channel constant fraction discriminator and coincidence unit (MCFD-16; Mesytec, Putzbrunn, Germany). The MCFD-16 is capable of user-configurable specification of which particular detector modules can form a valid coincidence pair with any other given detector. When there is at least one pair of anode pulses from a valid detector pair falling within the preset coincidence timing window, an output trigger pulse initiating digitization of the position encoding signals is sent from the MCFD-16 to the AiT ADC unit (Figure 3). Energy discrimination for each detector of a coincidence pair is based on the sum of its two largest digitized position-encoding signals. It is performed during playback of the list-mode data during image reconstruction using user-specified energy window settings.

Increasing the number of allowed detector pairs increases the rate of detection of true events, but also increases the randoms rate, which is also sensitive to the width of

the coincidence timing window. As part of this study, tests were performed to identify the optimal number of coincidence pairs, as well as the coincidence widow width. Both parameters were systematically varied to identify values that maximized the system noise equivalent count rate (NECR), as follows. The number of coincident pairs for the nth detector module was increased in steps, starting from the minimum value of one (paired with only the n + 6th module directly opposing it in the ring). At each step, the number of additional coincidence modules, i, on each side of the central opposing module was incremented by one. The timing window width was varied at each step to obtain the maximum NECR. The results are shown in Table 1.

Table 1. NECR for varying coincidence pair number and timing window width.

Number of Adjacent Detectors, *i*	Timing Window (ns)	Peak NEC Rate (kcps)
1	8	2.77 (16 MBq)
	10	3.87 (19 MBq)
	12	4.28 (18 MBq)
2	8	4.11 (18 MBq)
	10	4.69 (20 MBq)
	12	5.33 (21 MBq)
3	8	1.56 (18 MBq)

Images are reconstructed using a maximum likelihood expectation maximization (MLEM) algorithm with 10 iterations, using 1 mm cubic voxels [17]. Attenuation correction was performed assuming uniform attenuation throughout the volume of the breast, with a linear attenuation coefficient equal to that of water at 511 keV; μ_{water} = 0.096 cm^{-1}. This value was chosen because of its close similarity to the attenuation coefficient of 50/50 fibroglandular/adipose breast tissue (μ_{breast} = 0.098 cm^{-1} at 511 keV) [18].

2.2. Imaging Performance

There are currently no National Electrical Manufacturers Association (NEMA) standards designed specifically for measurement of dbPET scanner imaging performance so, consistent with the dbPET literature, we have followed a modified version of the NEMA NU 4-2008 protocol, developed for preclinical PET [13,14,19]. Unless otherwise noted all basic imaging performance evaluation described below followed that protocol.

2.3. Energy Resolution

A line source phantom was filled with 18.5 MBq of FDG and placed in the center of the VoV. Counts were acquired for 30 min. Separate energy spectra for every crystal of each module (total of 5808 crystals) were produced. A global energy spectrum was obtained by summing the normalized individual crystal spectra, following scaling of their energy bin values to place their peaks at the same bin. The summed energy histogram was then fitted to the sum of two Gaussian curves, utilizing MATLABs "gauss2" fit function. The energy resolution was calculated as the full width at half maximum (FWHM) of the Gaussian centered on the photopeak, divided by the Gaussian peak location, and expressed as a percentage.

2.4. Spatial Resolution

A 1 mm diameter Na-22 source (Eckert & Ziegler Isotope Products, Valencia, CA, USA, Model: MMS03-022) with an activity of 0.37 MBq was imaged for 5 min at radial distances of 0, 20, 40, 60 and 75 mm from the center of the VoV. The response function of each reconstructed image was measured along the axial, radial, and transverse directions [19]. In a departure from the parabolic interpolations used in the NEMA protocol, the profiles

were fitted to a Gaussian curve, and the spatial resolution was defined as the FWHM of the fit.

2.5. System Sensitivity

System sensitivity is defined as the background-subtracted coincidence rate for a given source strength and branching ratio [19]. The Na-22 point source used in the measurement of the spatial resolution was again used, and the energy window was set at +/− 10% (460–562 keV) [19].

2.6. Count Rate and Scatter Fraction

A primary figure of merit in PET imaging is the noise equivalent count rate (NECR), which is the ratio of the true coincidence rate to the sum of the true, random, and scatter rates. It is proportional to the square of the image SNR and is positively and significantly related to clinically perceived PET image quality [20]. The measurements of both the NECR and scatter fraction followed the NEMA NU-2 (whole body PET) and NU-4 protocols but used a modified phantom with a size appropriate for breast imaging.

The phantom design is similar to the one created by Moliner et al. [12] and filled with a known activity of F-18 solution (350 MBq, resulting in 21 MBq/cm). The filled phantom was placed at the center of the VoV such that the transaxial mid-plane bisected the center of the cylindrical phantom. Data were acquired every 25 min with 10 min acquisitions until the calculated tube activity was below 10 MBq. Data were then analyzed according to the NEMA NU-4-2008 protocol [19]. NECR and scatter fraction analyses were performed using the same dataset.

2.7. Vertical Extent of VoV and Image Quality for Posterior Tissue Imaging

Two experiments were designed to measure how high the BRPET scanner's VoV extends relative to the top surface of the examination table's 3.35 mm thick breast aperture. The aperture's top surface defines the location of the subject's chest wall, and thus the location of the most posterior portion of the breast.

The first experiment utilized two capillary tubes placed at a 43.6° angle relative to each other with their intersection placed at the height of the top (most posterior) surface of the aperture (Figure 1). Each capillary tube was filled with ~0.37 MBq of FDG. The phantom was scanned for 10 min. In each of the transaxial image slices a profile running through the center of both capillary tubes was extracted and Gaussian fits to the peaks were used to determine the capillary separation. The slice-by-slice capillary separations were extrapolated to zero to provide the distance between the most posterior slice in which both tubes could be clearly visualized and the posterior aperture surface.

Second, to characterize the scanner's useful vertical (z-dimension) field of view under more realistic breast imaging conditions with low contrast lesions, a fillable breast phantom containing an FDG solution with a concentration of ~0.037 MBq/mL, and a simulated lesion was used. The lesion had an internal diameter of either 0.8 or 1.2 cm, and a lesion-to-background activity ratio (LBR) of either 2.1 or 3.1 (Table 2). These LBRs were chosen to replicate the low-end of reported lesion-to-background FDG uptake ratios for breast cancer [21,22]. For each lesion, the phantom was positioned so that the lesion was at the center of the VoV of the BRPET ring as determined by the high contrast VoV extent study. The ring was translated downward in 2 mm increments, with five-minute acquisitions at each position, until the lesion was completely out of the scanner's high contrast VoV. For each lesion size, activity concentration, and ring position, the lesion SNR was measured in the reconstructed transaxial image slice centered on the lesion. Lesion SNR was defined as:

$$\mathrm{SNR} = \frac{\left(\mathrm{N_l} - \mathrm{N_{bg}}\right)}{\sigma_{\mathrm{bg}}} \quad (1)$$

where N_l is the average voxel value in a circular region of interest (ROI) centered on the lesion, N_{bg} is the average voxel value in a similar size toroidal ROI in the nearby background region and centered on the lesion (Figure 4), and σ_{bg} is the standard deviation of the voxel values in the background ROI.

Table 2. Activity concentrations used in SNR phantom experiments. * Lesion-to-Background Ratio.

Lesion Diameter (cm)	Lesion Concentration (kBq/mL)	Background Concentration (μCi/mL)	LBR *
1.2	113.2	38.1	3.1
1.2	75.5	37.7	2.1
0.8	129.5	41.8	3.1
0.8	80.3	38.1	2.1

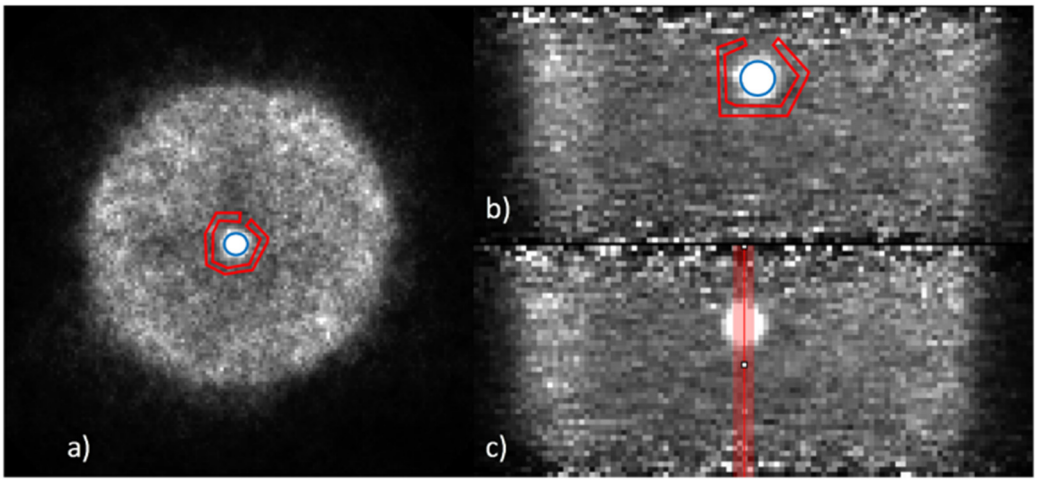

Figure 4. ROIs used to calculate the SNR. The average lesion voxel value is calculated from the ROI in blue in Figure (**a**,**b**), while the average background voxel value is calculated from the ROI in red. Figure (**c**) shows the profile used to measure the z-position of the lesion within the VoV.

2.8. Pilot Human Study

A pilot human study was performed comparing clinical contrast enhanced MRI (CE-MRI) to BRPET in terms of lesion sensitivity and specificity. Subjects were scanned under a protocol approved by the institutional review board of the University of Virginia's School of Medicine (IBR# 18406). All study information was handled in compliance with the rules and regulations of the Health Insurance Portability and Accountability Act. Eligible subjects were females 18 years of age or older who were not pregnant, not breast feeding, and who were either scheduled for a clinical CE-MRI breast scan, or who had had a recent CE-MRI breast scan. A total of 10 subjects were scanned with a total of 11 biopsied lesions.

After informed consent, each subject was intravenously injected with ~222 MBq of ^{18}FDG, resulting in a total body effective dose of 4.2 mSv, versus the standard dose of ~10.5 mSv [23]. Following a 45 min uptake period each breast was scanned, starting with the suspicious breast. The PET ring was initially positioned as close to the chest wall as possible and then was moved down in 3 cm steps until the entire breast was covered. The somewhat conservative step size of 3 cm was selected to allow a 2 cm overlap of the 5 cm axial fields of view to maintain relatively constant photon sensitivity throughout the scan. Data were acquired for 5 min at each ring position. For the 19 breasts imaged, the average (SD) number of ring positions, scan time, and injected activity were 3.6 (0.74), 18.1 (3.70) min, and 213 (32.8) MBq, respectively. The final BRPET images were interpreted by two board-certified nuclear medicine radiologists who were blinded to all background

clinical information. The CE-MRI results were read by an MQSA-certified breast radiologist with 5 years of experience in clinical breast MRI. Readers were asked to rank the quality of each image as: (1) not adequate, (2) barely adequate, (3) adequate, (4) good, or (5) excellent. Readers were then asked to localize any suspicious findings and score each finding on a linear 1–5 suspicion scale (1—definitely benign, 2—probably benign, 3—indeterminate, 4—probably malignant, 5—definitely malignant). Reader results were used to calculate sensitivity, specificity, positive predictive value (PPV), and accuracy for each finding, taking biopsy results as ground truth for malignancy (Equations (2)–(5)).

$$\text{Sensitivity} = \frac{\text{True Positive}}{\text{True Positive} + \text{False Negative}} \tag{2}$$

$$\text{Specificity} = \frac{\text{True Negative}}{\text{True Negative} + \text{False Positive}} \tag{3}$$

$$\text{PPV} = \frac{\text{True Positive}}{\text{True Positive} + \text{False Positive}} \tag{4}$$

$$\text{Accuracy} = \frac{\text{True Positive} + \text{True Negative}}{\text{True Positive} + \text{False Positive} + \text{False Negative} + \text{True Negative}} \tag{5}$$

The subjects in this study were recruited from among women undergoing UVa's routine clinical contrast–enhance breast MRI protocol, and these clinical images were used in the comparison with BRPET. The MRI scans were performed on a Siemens Espree 1.5 Tesla scanner (Siemens Healthineers, Erlangen, Germany). The contrast enhanced portion of the protocol included one pre- and three post-contrast axial 3D T1 Dixon dynamic sequences, and one post-contrast axial 3D T1 Dixon high resolution scan. The contrast scans were conducted with 10 mL of Gadavist contrast agent (Bayer Healthcare, Whippany, NJ, USA). In addition to these post-contrast scans, two pre-contrast scans (one T2-weighted and one T1-weighted) are also routinely obtained as part of the standard-of-care breast MRI protocol at our institution, and these were also made available to the readers. The list of sequences, along with their pre- or post-contrast status, is shown in Table 3 and the histological results of the subjects' biopsies can be seen in Table 4.

Table 3. Sequence names and parameters used for the clinical MRI study including the CE-MRI study.

Sequence Name	Number of Scans	Voxel Size (mm^3)	Slice Thickness (mm)	TR (ms)	TE 1 (ms)	TE 2 (ms)	Flip Angle (degrees)	Gadolinium Contrast Injection
Axial T2 FS Dixon	1	$0.8 \times 0.8 \times 3.0$	3	5630	81	N/A	165	pre
Axial T1 3D	1	$0.8 \times 0.8 \times 1.3$	1.3	6.03	2.57	N/A	20	pre
Axial 3D T1 Dixon Dynamic	4	$0.8 \times 0.8 \times 1.3$	1.3	5.67	2.46	3.69	14	1 pre/3 post
Axial 3D T1 Dixon High Resolution	1	$0.9 \times 0.9 \times 0.8$	0.8	5.67	2.46	3.69	14	post

Table 4. Histological results of lesions biopsied.

Tumor Status and Type	Number of Lesions
Benign	
Lobular Carcinoma in situ	1
Fibroadenoma	1
Stromal Fibrosis	1
Fat Necrosis	1
Malignant	
Infiltrating Ductal Carcinoma	5
Infiltrating Lobular Carcinoma	2

3. Results

3.1. Energy Resolution

The energy resolution calculated from the spatially averaged energy histogram was 21.2% FWHM.

3.2. Spatial Resolution

Figure 5 plots the FWHM of the reconstructed image of the 1 mm Na-22 point source as the source was translated within the central plane of the ring and within a plane at one quarter of the ring height (Figure 2b). In the center plane the axial, radial, and tangential resolutions at the center of the VoV were 1.8, 1.7, and 1.9 mm, respectively. In the quarter-ring-height plane the spatial resolution in all three dimensions is comparable near the radial center, but due to depth of interaction uncertainty (parallax), degradation is observed in the radial FWHM resolution.

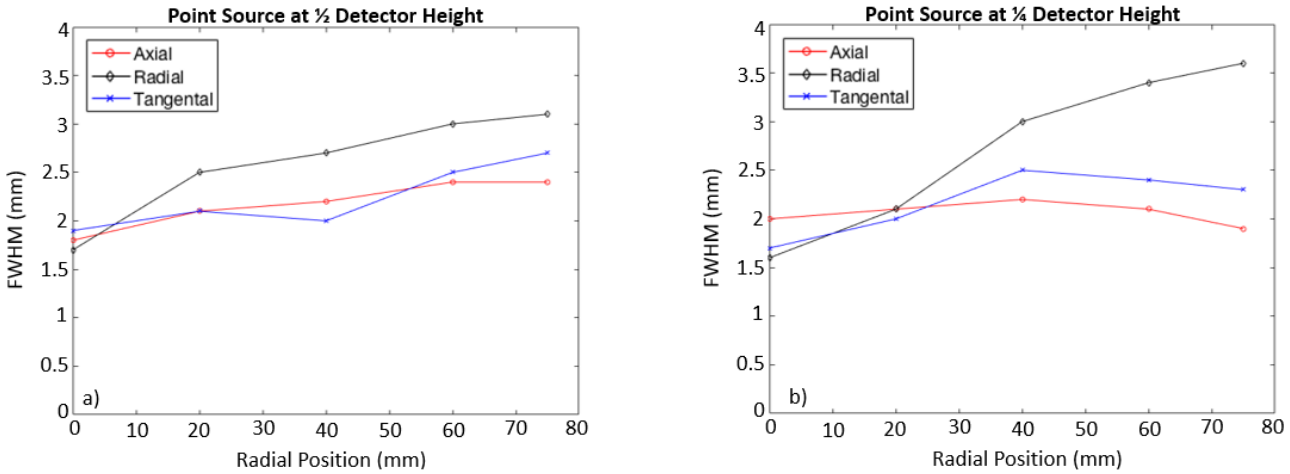

Figure 5. Plots showing the spatial resolution as the point source is moved from the center of VoV to the edge of the VoV. The top graph is for source locations in the ring's central plane, and the bottom graph is for source locations in a parallel plane, 1.25 cm from the central plane.

3.3. System Sensitivity

The shape of the system's sensitivity profile along the ring's axial dimension was triangular as expected, with the peak sensitivity occurring in the center of the axial dimension. At the ring isocenter the peak absolute sensitivity is 0.97%. The total system absolute sensitivity, calculated by summing over all transverse slices in the VoV, is 19.3%.

3.4. Count Rate and Scatter Fraction

Figure 6 shows, for a timing window of 12 ns and with coincidences permitted only between a module and its five most directly opposing modules, the relationships between the NEC rate and the true, random, and scatter rates as the activity increases. The maximum NECR was 5.33 kcps at 21.6 MBq FDG. The scatter fraction was calculated to be 29.8%.

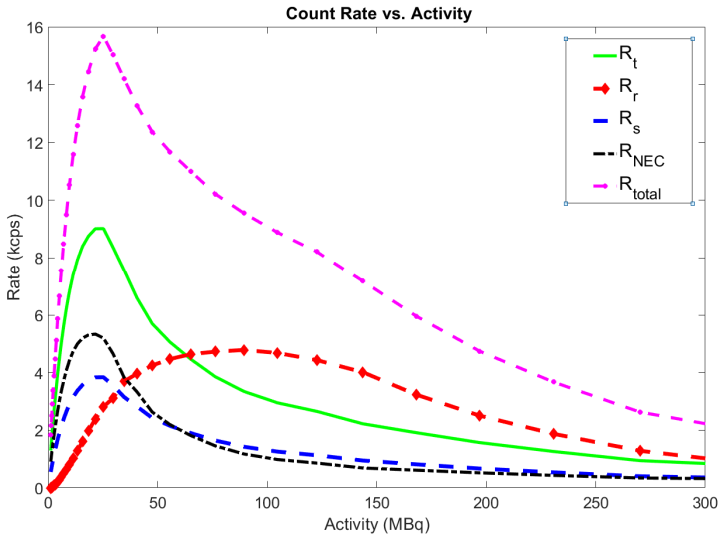

Figure 6. Counting rate performance versus source activity. R_t = true rate; R_r = random rate; R_s = scatter rate; R_{NEC} = noise equivalent count rate; R_{tot} = total count rate.

3.5. Image Quality for Posterior Tissue Imaging

Extrapolation to zero of the transaxial slice peak-to-peak separation of the two capillary tubes showed that the capillary intersection, and thus the horizontal plane containing the posterior surface of the breast aperture, was slightly more than six slices above the highest slice in which both capillaries were clearly visible. Thus the vertical distance between the top surface of the breast aperture and the topmost plane of the VoV was determined to be 6.3 mm.

The results of the low SNR assessment of the posterior limit of the VoV are shown in Figure 7, where lesion SNR is plotted versus the vertical distance between the lesion center and the top surface of the breast aperture, for each of the four lesion diameters and LBRs tested. For each curve, the leftmost (i.e., smallest lesion depth) point plotted indicates the lesion SNR at the uppermost 3 cm ring step position at which that lesion was still visible in the reconstructed image. The figure shows that for the low lesion LBR values tested none of the lesions were visible at the anterior limit of the VoV identified in the high contrast capillary experiment.

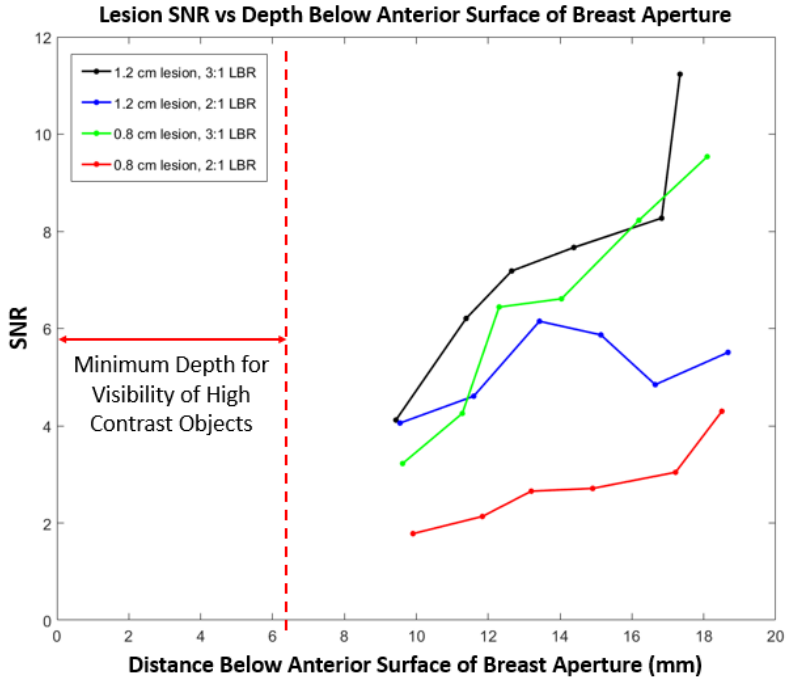

Figure 7. Lesion SNR versus lesion depth below the top surface of the breast aperture. The vertical red line shows the minimum depth for visibility of high contrast objects (i.e., large or high-LBR lesions).

3.6. Pilot Human Study

Of the 11 biopsied lesions, 7 were malignant and 4 were benign. The clinical MRI reports of two subjects showed that they had no suspicious findings that would lead to a biopsy.Table 5 compares the sensitivity, specificity, PPV, and accuracy of the BRPET to those of CE-MRI under two possible suspicion threshold conditions: (a) findings with a malignancy suspicion score of $\geq$3 were considered positive and (b) lesions with a malignancy suspicion score of $\geq$4 were considered positive. Figure 8 shows a transverse slice containing a large cancer easily detected by both modalities.

Table 5. Performance metrics for human trial. NM 1 and 2 are nuclear medicine radiologist readers; BR is a breast radiologist reader. PPV = positive predictive value.

Modality	**BRPET**		**CE-MRI**	**BRPET**		**CE-MRI**
Reader	NM 1	NM 2	BR	NM 1	NM 2	BR
	Suspicion score $\geq$3 is positive			Suspicion score $\geq$4 is positive		
Sensitivity (%)	100	100	100	85.7	100	100
Specificity (%)	100	100	25	100	100	25
PPV (%)	100	100	70	100	100	70
Accuracy (%)	100	100	72.7	90.9	100	72.7

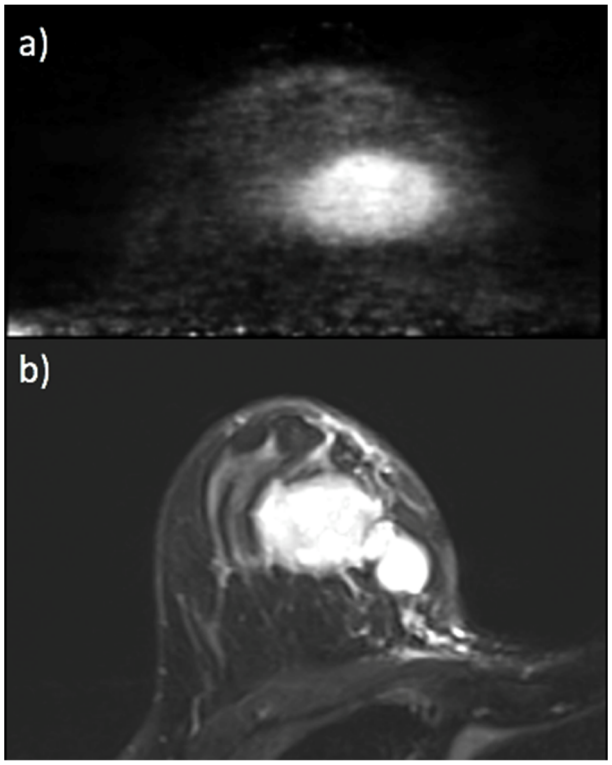

Figure 8. (**a**) BRPET scan of the right breast of a subject with a known malignancy originally seen on a 2D mammogram and then staged with CEMRI, seen in (**b**). The image comparison in this case strongly suggests that the base of the breast is visible in the PET image.

4. Discussion

The BRPET system was designed with a primary goal of improving visualization of posterior breast tissue compared to other systems for dbPET, while maintaining the spatial resolution and system sensitivity of comparable single ring systems [12,13]. The results reported here indicate that in terms of the posterior limit of the VoV and spatial resolution these goals were reached.

The measured spatial resolution of BRPET is comparable to that of other dbPET systems [12,13,24] (Table 6), and like that of the other dedicated systems, is superior to that of WBPET (FWHM transaxial and axial resolutions 1 cm from isocenter of 4.3–5.8 mm and 4.1–4.2 mm, respectively) [25]. Figure 4 shows that the full ring geometry of BRPET also enables nearly isotropic spatial resolution near the center of the VoV. This is unlike limited angle dbPET systems for which the resolution in one of the three dimensions is much poorer than in the other two. For planes midway between the ring's central and peripheral planes the BRPET tangential resolution is somewhat degraded towards the VoV periphery, while the axial and radial resolutions remain nearly constant.

The highest photon sensitivity in any PET system is at the center of the VoV, where the number of geometrically possible lines of response is greatest. As anticipated, the BRPET sensitivity falls approximately linearly as a function of the axial distance from the ring's central plane. The peak sensitivity is lower than that reported for the MAMMI system (0.97 and 1.8% peak for BRPET and MAMMI, respectively), while the total system sensitivity is comparable (19.3 and 20%, respectively) [12].

The results of the VoV experiments showed that under high contrast conditions (e.g., high lesion uptake and/or high LBR) the BRPET system is capable of imaging tissue up to within ~6 mm of the top surface of the table's breast aperture. However, as shown in Figure 6, detection of small or low uptake lesions presents a more difficult imaging challenge in terms of SNR. The lesions used in the breast phantom study were intentionally chosen to have very low LBR (~2 to 3) compared to what would be encountered clinically

(~17 for ductal cancer and ~6 for lobular cancer) [22]. Since the numerator of the lesion SNR varies approximately proportionally with the LBR, Figure 6 suggests that at a depth of 10 mm even the smallest (0.8 mm diameter) lesion tested would, with an LBR of 6.5, have an SNR of approximately 6.2, making it readily visible.

Table 6. Comparison of key imaging performance metrics of BRPETamong compared to those of several commercial dbPET scanners.

Author	System	Axial Resolution (mm)	Transaxial Resolution (mm)	Total Sensitivity (%)	Maximum NECR (kcps)
This work	BRPET	1.8	1.9	0.97 (460–562 keV)	5.33 (21 MBq)
Luo et al. (ref. [24])	Naviscan	6.2	1.8	18 (350–700 keV)	10.6 (25 MBq)
Wu et al. (ref. [9])	2-camera PET	2.17	2.7	1.64 (350–650 keV)	19.3 (11.8 MBq)
Moliner et al. (ref. [13])	MAMMI PET	1.6	1.9	20 (250–750 keV)	25 (44 MBq)
Miyake et al. (ref. [14])	Shimadzu Full-Ring PET	1	0.7	16.3 (100–800 keV)	300 (44 MBq)

To our knowledge, neither high contrast nor SNR-based analysis of the posterior extent of the usable VoV of other dbPET scanners is available in the literature, making direct comparison difficult. In a study of 230 subjects undergoing both whole body PET (WBPET) and MAMMI, with WBPET findings used as ground truth, the MAMMI system had a lesion detection sensitivity of 88.9%. However, when tumors outside the scanner's VoV near the chest wall were excluded from the analysis, the sensitivity increased to 98.6% [26]. A more recent study of MAMMI also concluded that lack of visualization of posterior breast tissue degraded BIRADS-4 lesion sensitivity [27]. Investigators at the Mayo Clinic reported significant gains in the volume of posterior breast tissue imaged by MAMMI via modification of its standard table to provide a larger breast aperture and thinner table sections [28].

In a study including 69 subjects, WBPET was compared to both Shimadzu's full-ring O scanner and to their C-shaped scanner. The overall lesion sensitivities of the O and C scanners were 82 and 83%, respectively. However, excluding lesions outside of their VoVs their sensitivities increased to 93 and 90%, respectively [11]. The authors of this study noted that all tumors outside of the field of view were located close to the chest wall in the posterior breast tissue [11].

It should be noted that the conical recess of the prone table breast aperture produces a natural convex flexing downward of the chest wall region, with the result that some posterior breast tissue extends lower than the plane defined by the edges of the breast aperture.

Participants in the pilot human study comparing BRPET to CEMRI were primarily women with recently diagnosed breast cancer (n = 8) and high-risk women undergoing breast cancer screening with CEMRI (n = 2). Among this cohort, the sensitivity of BRPET was comparable to that of CEMRI while the specificity was ~4-fold higher and the overall accuracy was ~25% higher (see Table 5). The lower specificity for CEMRI was due to a large number of false positives. These results suggest that BRPET might have a role in reducing the false positive rate of CEMRI without unacceptably increasing the false negative rate.

Although the performance of the BRPET scanner was encouraging, there is room for improvement. Most importantly, the NECR of 5.3 kcps at 21 MBq, although adequate for the human study described here, is lower than desirable. It is limited primarily by inefficiencies and overhead in the data acquisition software, which must be replaced in order to increase count rate capability, and thus improve photon sensitivity and image SNR. Also, the addition of a second detector ring could increase the axial FoV sufficiently to permit the majority of breasts to be imaged with only one or two vertical detector posi-tions, thereby decreasing scan time and improving overall scanner sensitivity.

5. Conclusions

The physical characterization of the BRPET prototype showed that its VoV extends well into the breast aperture, to within ~6 mm of the plane in which the most posterior (chest wall) region of the breast lies, thereby providing excellent access to posterior breast tissue. The spatial resolution of the BRPET prototype is nearly isotropic and is comparable to that of commercial dbPET systems and superior to that of commercial WBPET scanners. Acquisition electronics count rate limitations result in a peak 5.33 kcps at 21 MBq. The pilot human evaluation of the BRPET system suggest substantially improved specificity and moderately higher PPV compared to CEMRI; however, larger human studies are necessary to better quantify these differences.

Author Contributions: Conceptualization, A.M.P., M.B.W., S.M., A.V.S., P.K.R., P.M.D.; methodology (system characterization), A.M.P. and M.B.W.; software, A.V.S., S.M.; validation, A.M.P., M.B.W. and A.K.K.; formal analysis, A.M.P. and M.B.W.; investigation, A.M.P., A.K.K., M.B.W., P.K.R., L.L., H.R.P. and P.M.D.; resources, A.M.P., M.B.W., A.V.S., S.M.; data curation, A.M.P. and M.B.W.; writing—original draft preparation, A.M.P.; writing—review and editing, A.M.P., A.K.K., M.B.W., P.K.R., L.L., H.R.P., P.M.D., S.M. and A.V.S.; supervision, M.B.W.; project administration, M.B.W.; funding acquisition, M.B.W., P.K.R., and P.M.D. All authors have read and agreed to the published version of the manuscript.

Funding: This research was supported by the UVa Cancer Center through the NCI Cancer Center Support Grant P30 CA44579 and support from the Commonwealth of Virginia.

Institutional Review Board Statement: The study was conducted according to the guidelines of the Declaration of Helsinki, and approved by the Institutional Review Board of the University of Virginia (IRB protocol #18406).

Informed Consent Statement: Informed consent was obtained from all subjects involved in the study.

Data Availability Statement: Data available on request of corresponding authors.

Conflicts of Interest: The authors declare no conflict of interest.

References

1. Paydary, K.; Seraj, S.M.; Zadeh, M.Z.; Emamzadehfard, S.; Shamchi, S.P.; Gholami, S.; Werner, T.J.; Alavi, A. The Evolving Role of FDG-PET/CT in the Diagnosis, Staging, and Treatment of Breast Cancer. *Mol. Imaging Biol.* **2019**, *21*, 1–10. [CrossRef] [PubMed]
2. Wu, D.; Gambhir, S.S. Positron Emission Tomography in Diagnosis and Management of Invasive Breast Cancer: Current Status and Future Perspectives. *Clin. Breast Cancer* **2003**, *4* (Suppl. 1), S55–S63. [CrossRef] [PubMed]
3. Avril, N.; Adler, L.P. F-18 Fluorodeoxyglucose-Positron Emission Tomography Imaging for Primary Breast Cancer and Loco-Regional Staging. *Radiol. Clin. N. Am.* **2007**, *45*, 645–657. [CrossRef] [PubMed]
4. Weinberg, I.; Majewski, S.; Weisenberger, A.; Markowitz, A.; Aloj, L.; Majewski, L.; Danforth, D.; Mulshine, J.; Cowan, K.; Zujewski, J.; et al. Preliminary results for positron emission mammography: Real-time functional breast imaging in a conventional mammography gantry. *Eur. J. Nucl. Med.* **1996**, *23*, 804–806. [CrossRef] [PubMed]
5. MacDonald, L.; Edwards, J.; Lewellen, T.; Haseley, D.; Rogers, J.; Kinahan, P. Clinical Imaging Characteristics of the Positron Emission Mammography Camera: PEM Flex Solo II. *J. Nucl. Med.* **2009**, *50*, 1666–1675. [CrossRef] [PubMed]
6. Kalinyak, J.E.; Berg, W.A.; Schilling, K.; Madsen, K.S.; Narayanan, D.; Tartar, M. Breast cancer detection using high-resolution breast PET compared to whole-body PET or PET/CT. *Eur. J. Nucl. Med. Mol. Imaging* **2014**, *41*, 260–275. [CrossRef] [PubMed]
7. Eo, J.S.; Chun, I.K.; Paeng, J.C.; Kang, K.W.; Lee, S.M.; Han, W.; Noh, D.-Y.; Chung, J.-K.; Lee, D.S. Imaging sensitivity of dedicated positron emission mammography in relation to tumor size. *Breast* **2012**, *21*, 66–71. [CrossRef] [PubMed]
8. Wu, Y.; Bowen, S.L.; Yang, K.; Packard, N.; Fu, L.; Burkett, G.; Qi, J.; Boone, J.M.; Cherry, S.R.; Badawi, R.D. PET characteristics of a dedicated breast PET/CT scanner prototype. *Phys. Med. Biol.* **2009**, *54*, 4273. [CrossRef] [PubMed]
9. Raylman, R.R.; Majewski, S.; Smith, M.F.; Proffitt, J.; Hammond, W.; Srinivasan, A.; McKisson, J.; Popov, V.; Weisenberger, A.; Judy, C.O.; et al. The positron emission mammography/tomography breast imaging and biopsy system (PEM/PET): Design, construction and phantom-based measurements. *Phys. Med. Biol.* **2008**, *53*, 637–653. [CrossRef] [PubMed]
10. Kitamura, K.; Ohi, J.; Tonami, H.; Yamada, Y.; Furumiya, T.; Furuta, M.; Satoh, M.; Tsuda, T.; Nakazawa, M.; Hashizume, N.; et al. Development of a C-shaped breast PET scanner equipped with four-layer DOI detectors. In Proceedings of the 2008 IEEE Nuclear Science Symposium Conference Record, Dresden, Germany, 19–25 October 2008; pp. 5662–5665.
11. Iima, M.; Nakamoto, Y.; Kanao, S.; Sugie, T.; Ueno, T.; Kawada, M.; Mikami, Y.; Toi, M.; Togashi, K. Clinical performance of 2 dedicated PET scanners for breast imaging: Initial evaluation. *J. Nucl. Med.* **2012**, *53*, 1534–1542. [CrossRef] [PubMed]

12. Moliner, L.; González, A.J.; Soriano, A.; Sánchez, F.; Correcher, C.; Orero, A.; Carles, M.; Vidal, L.F.; Barberá, J.; Caballero, L.; et al. Design and evaluation of the MAMMI dedicated breast PET. *Med. Phys.* **2012**, *39*, 5393–5404. [CrossRef] [PubMed]
13. Miyake, K.K.; Matsumoto, K.; Inoue, M.; Nakamoto, Y.; Kanao, S.; Oishi, T.; Kawase, S.; Kitamura, K.; Yamakawa, Y.; Akazawa, A.; et al. Performance Evaluation of a New Dedicated Breast PET Scanner Using NEMA NU4-2008 Standards. *J. Nucl. Med.* **2014**, *55*, 1198–1203. [CrossRef] [PubMed]
14. Masumoto, N.; Kadoya, T.; Fujiwara, M.; Murakami, C.; Yoshikawa, T.; Handa, Y.; Amioka, A.; Gohda, N.; Kono, M.; Sasada, S.; et al. Dedicated breast PET to improve clinical diagnosis of breast cancer: Initial evaluation. *JCO* **2017**, *35*, e12097. [CrossRef]
15. Majewski, S. High Resolution PET Breast Imager with Improved Detection Efficiency. 2010. Available online: https://patents.google.com/patent/US7732774B2/en (accessed on 30 July 2018).
16. Popov, V.; Majewski, S.; Weisenberger, A.G. Readout electronics for multianode photomultiplier tubes with pad matrix anode layout. In Proceedings of the 2003 IEEE Nuclear Science Symposium Conference Record (IEEE Cat No03CH37515), Portland, OR, USA, 19–25 October 2003; Volume 3, pp. 2156–2159.
17. Smith, M.F.; Raylman, R.R. PEM-PET Image Reconstruction in a Clinically-Relevant Time Frame. In Proceedings of the 2006 IEEE Nuclear Science Symposium Conference Record, San Diego, CA, USA, 29 October–1 November 2006; pp. 1792–1796.
18. International Commission on Radiation Units and Measurements. Tissue substitutes in radiation dosimetry and measurement. In *ICRU Technical Report No. 44*; ICRU: Bethesda, MD, USA, 1989.
19. Performance Measurements of Small Animal Positron Emission Tomographs (PETs). Available online: https://www.nema.org/Standards/Pages/Performance-Measurements-of-Small-Animal-Positron-Emission-Tomographs.aspx (accessed on 13 January 2017).
20. Queiroz, M.A.; Wollenweber, S.D.; von Schulthess, G.; Delso, G.; Veit-Haibach, P. Clinical image quality perception and its relation to NECR measurements in PET. *EJNMMI Phys.* **2014**, *1*, 1–13. Available online: https://www.ncbi.nlm.nih.gov/pmc/articles/PMC4546067/ (accessed on 28 May 2019).
21. Avril, N.; Bense, S.; Ziegler, S.I.; Dose, J.; Weber, W.; Laubenbacher, C.; Römer, W.; Jänicke, F.; Schwaiger, M. Breast imaging with fluorine-18-FDG PET: Quantitative image analysis. *J. Nucl. Med.* **1997**, *38*, 1186–1191. [PubMed]
22. Buck, A.; Schirrmeister, H.; Kühn, T.; Shen, C.; Kalker, T.; Kotzerke, J.; Dankerl, A.; Glatting, G.; Reske, S.; Mattfeldt, T. FDG uptake in breast cancer: Correlation with biological and clinical prognostic parameters. *Eur. J. Nucl. Med.* **2002**, *29*, 1317–1323. [CrossRef] [PubMed]
23. ICRP. ICRP Publication 106. Available online: http://www.icrp.org/publication.asp?id=ICRP%20Publication%20106 (accessed on 22 July 2018).
24. Luo, W.; Anashkin, E.; Matthews, C.G. Performance Evaluation of a PEM Scanner Using the NEMA NU 4 #x2014; 2008 Small Animal PET Standards. *IEEE Trans. Nucl. Sci.* **2010**, *57*, 94–103.
25. Slomka, P.J.; Pan, T.; Germano, G. Recent Advances and Future Progress in PET Instrumentation. *Semin. Nucl. Med.* **2016**, *46*, 5–19. [CrossRef] [PubMed]
26. Teixeira, S.C.; Rebolleda, J.F.; Koolen, B.B.; Wesseling, J.; Jurado, R.S.; Stokkel, M.P.M.; Santiago, M.D.P.C.; Van Der Noort, V.; Rutgers, E.J.T.; Olmos, R.A.V. Evaluation of a Hanging-Breast PET System for Primary Tumor Visualization in Patients With Stage I–III Breast Cancer: Comparison With Standard PET/CT. *Am. J. Roentgenol.* **2016**, *206*, 1307–1314. [CrossRef] [PubMed]
27. Graña-López, L.; Herranz, M.; Domínguez-Prado, I.; Argibay, S.; Villares, A.; Ruibal, A.; Vázquez-Caruncho, M. Dedicated breast PET value to evaluate BI-RADS 4 breast lesions. *Eur. J. Radiol.* **2018**, *108*, 201–207. [CrossRef] [PubMed]
28. O'Connor, M.K.; Tran, T.D.; Swanson, T.N.; Ellingson, L.R.; Hunt, K.N.; Whaley, D.H. Improved visualization of breast tissue on a dedicated breast PET system through ergonomic redesign of the imaging table. *EJNMMI Res.* **2017**, *7*, 1–9. Available online: https://www.ncbi.nlm.nih.gov/pmc/articles/PMC5736520/ (accessed on 24 November 2018). [CrossRef] [PubMed]